Seismic Evidence of the Transition from Debris Flow to Hyperconcentrated Flow at Mount Rainier, USA

OPEN ACCESS

Katherine M. Biegel[*1], Elaine A. Collins[2], Kate E. Allstadt[2], Avery Conner[3], Amanda M. Thomas[1], Weston Thelen[4], Alexandra M. Iezzi[4], Scott Beason[5], and Claire Todd[6]

Abstract

Debris flows are a seasonal hazard in Tahoma Creek in Mount Rainier National Park, Washington, United States. We present seismic recordings spaced every 100–200 m along the path of a debris flow triggered by a glacial outburst on 15 August 2023. These recordings capture changes as the debris flow deposits ~24,000 cubic meters of material along an ~800 m stretch of channel, approximately 2.5 km from the glacial source. As the flow deposits material, the seismic signal onset shape associated with the debris flow snout recedes, resulting in an elongation of the delay between the signal onset and the peak amplitude from 100 to 300 s. In parallel, the peak frequency increases by more than 20 Hz, and energy below 20 Hz fades, indicating deposition of larger particles and changes in sediment concentration within the flow. We interpret these changes to correspond to the transition from debris flow to hyperconcentrated flow, a distinction based on sediment concentration by volume and on rheological criteria such as yield strength. We find that the frequency content of the seismic signal depends on grain size and sediment concentrations within the flow, among other factors, complicating the starting assumptions of many physical models of debris flows.

Cite this article as Biegel, K. M., E. A. Collins, K. E. Allstadt, A. Conner, A. M. Thomas, W. Thelen, A. M. Iezzi, S. Beason, and C. Todd (2026). Seismic Evidence of the Transition from Debris Flow to Hyperconcentrated Flow at Mount Rainier, USA, *Seismol. Res. Lett.* **XX**, 1–13, doi: 10.1785/0220260021.

Supplemental Material

Introduction

Debris flows and hyperconcentrated flows are high-discharge, sediment-rich flows that occur in steep channels and form a continuum of behavior controlled by sediment concentration, grain-size distribution, and yield strength (Iverson, 1997). Debris flows are characterized by a greater concentration of suspended sediment by volume than hyperconcentrated flows (>60% compared to 30%–60%; Beverage and Culbertson, 1964; Pierson, 2005). Because of the higher suspended particle concentration, debris flows have sufficient critical yield strength for gravel-sized particles to remain suspended in the flow (Hampton, 1975; Pierson and Costa, 1987) and represent the more energetic end of the continuum that includes hyperconcentrated flows, elevated streamflow, and regular streamflow. Flow events in steep channels, such as those at Mount Rainier, often begin as elevated streamflow and transition into debris flows as they entrain sediments and accelerate downhill, producing dense, unstratified mixtures that exceed 60% sediment by volume (Iverson, 1997; Pierson, 2005).

Debris flows and hyperconcentrated flows have complex seismic source mechanisms, where the signal can be considered comprised of energy from various processes like collisions of the flow particles with the channel bed (Hsu *et al.*, 2011; Schmandt *et al.*, 2013; Lai *et al.*, 2018; Farin *et al.*, 2019; Zhang *et al.*, 2021), flow dynamics such as turbulent flow (Gimbert *et al.*, 2014) or waves along the free surface (Belli *et al.*, 2022, 2025), and the seismic noise of the water itself (Schmandt *et al.*, 2013). In addition to these complex source dynamics, the signal's frequency and amplitude depend on particle collisions, sediment concentration, sediment grain size, both channel and station geometry, flow size or discharge, and fluid composition. Peak seismic amplitude has been shown to

1. Department of Earth and Planetary Science, University of California Davis, Davis, California, U.S.A., https://orcid.org/0000-0001-8682-6169 (KMB); https://orcid.org/0000-0001-6997-3140 (AMT); 2. U.S. Geological Survey, Geological Hazards Science Center, Golden, Colorado, U.S.A., https://orcid.org/0000-0002-5475-4022 (EAC); https://orcid.org/0000-0003-4977-5248 (KEA); 3. Department of Earth Sciences, University of Oregon, Eugene, Oregon, U.S.A., https://orcid.org/0009-0006-3142-9346 (AC); 4. U.S. Geological Survey, Volcano Science Center, Cascades Volcano Observatory, Vancouver, Washington, U.S.A., https://orcid.org/0000-0003-2534-5577 (WT); https://orcid.org/0000-0002-6782-7681 (AMI); 5. Mount Rainier National Park, National Park Service, Washington, U.S.A., https://orcid.org/0000-0003-0486-0094 (SB); 6. Department of Geological Sciences, California State University San Bernardino, San Bernardino, California, U.S.A., https://orcid.org/0000-0003-0545-6341 (CT)

*Corresponding author: kmbiegel@ucdavis.edu

Copyright © 2026. The Authors. This is an open access article distributed under the terms of the CC-BY license, which permits unrestricted use, distribution, and reproduction in any medium, provided the original work is properly cited.

Downloaded from pubs.geoscienceworld.org/ssa/srl/article-pdf/doi/10.1785/0220260021/8435001/srl-2026021.1.pdf by guest on 06 November 2026

correlate with peak flow discharge (Doyle *et al.*, 2010; Andrade *et al.*, 2022) and with front location and velocity (Walter *et al.*, 2017), flow height (Belli *et al.*, 2022) or volume (de Haas *et al.*, 2021; Zhang *et al.*, 2021), and mass flux (Belli *et al.*, 2022). Whereas the signal's frequency content may correlate with various flow behaviors (Schmandt *et al.*, 2013), source–receiver distance (Lai *et al.*, 2018), or sediment concentration (Márquez-Ramirez *et al.*, 2025). Increasing the size of particles within a debris flow is correlated with an increase in seismic ground velocity magnitude, but also correspondingly with increases in flow height and total volume, characteristics, which are difficult to isolate in natural flows (de Haas *et al.*, 2021).

Near-field seismic observations from various volcanic settings show that debris flows often generate more low-frequency seismic energy (<50 Hz) than hyperconcentrated flows due to the greater concentration of solids suspended in the flow and the grain size of the suspended particles themselves (Cole *et al.*, 2009; Doyle *et al.*, 2010). Debris flows form snouts, where larger-sized particles coalesce at the front of the flow, controlling flow speed (e.g., Takahashi, 2014). The signal associated with the debris flow snout exhibits higher seismic amplitudes than that of the following debris flow body (Kean *et al.*, 2015; Coviello *et al.*, 2019; Farin *et al.*, 2019; Belli *et al.*, 2026). Previous studies of near-channel seismic recordings have indicated that the peak frequency of debris flows lies in the 10–11 Hz range (Márquez-Ramirez *et al.*, 2025), likely generated from the stress of large blocks in the snout being dragged along the riverbed (Cole *et al.*, 2009; Yang *et al.*, 2024). As debris flows move down the channel, they may also form surge fronts, or internal waves. Surge fronts form through either progressive instabilities that form bores or roll waves, which increase in height and wave period with distance traveled until reaching a threshold defined by flow properties, or through regressive instabilities that arise from channel clogging or damming by large material (Zanuttigh and Lamberti, 2007). Surge fronts have coarser-grained material, control flow velocity, and exhibit higher seismic amplitudes than intersurge areas (Zanuttigh and Lamberti, 2007; Doyle *et al.*, 2010; Kean *et al.*, 2015; Coviello *et al.*, 2019; Belli *et al.*, 2026). Alternatively, the seismic dynamics of hyperconcentrated flows have been shown to depend more on viscous shear or turbulent stresses within the flow (Yang *et al.*, 2024). Previous studies have shown that the characteristic frequency of these flows is either bimodal or higher frequency than debris flows, with secondary peaks in the 21–23 Hz range (Márquez-Ramirez *et al.*, 2025).

Distinguishing between these flow types in natural settings is important for understanding entrainment and sedimentation processes, forecasting runout, and developing hazard-detection systems, especially at volcanoes where lahars pose a risk to downstream communities. Debris flows pose considerably higher hazard due to both their entrainment of larger particles and due to peak discharge being multiple times (2–60+) greater than water-dominated flows (Cavagnaro *et al.*, 2024). Seismic observations offer a promising tool for remotely identifying (Beason *et al.*, 2021; Kramer *et al.*, 2024) and tracking flows (Walter *et al.*, 2017), but interpreting these signals remains challenging because "near-field" recordings are rare, and there is no fully validated physical theory linking flow properties to seismic radiation (Allstadt *et al.*, 2018). In this instance, "near-field" refers to recordings in which the portion of the flow passing the station is the dominant feature in the seismic signal, and these recordings typically require the station to be within tens of meters of the debris flow channel (Allstadt *et al.*, 2018).

In this article, we present seismic evidence characterizing the transition from debris flow to hyperconcentrated flow that occurred during a debris flow on 15 August 2023, in Tahoma Creek, Mount Rainier National Park, Washington, United States (Fig. 1). The flow transition occurred over an ∼800 m reach where the channel starts to widen from a steep, narrow gorge to a broad, braided riverbed. By integrating seismic data with remote sensing observations and field photographs, we demonstrate that changes in the seismic signal reflect localized deposition and reductions in sediment concentration, providing evidence of the flow-style transition. These observations link channel geometry, sedimentation patterns, and seismic signatures, documenting how the seismic signals of debris flows evolve as they deposit material.

Study Area, Data, and Methods

Debris flows in Tahoma Creek

Mount Rainier, a stratovolcano in the Cascade Volcanic Arc, has a history of large lahars that have extended into the Puget Lowlands (Crandell, 1971; Hoblitt *et al.*, 1998). Lahars are debris flows or mudflows that occur exclusively in volcanic settings and can have sediment concentrations that span both debris flows and hyperconcentrated flows. Most of the large lahars at Mount Rainier can be linked to one of the 10–12 noteworthy eruptions within the last 2600 yr (Sisson and Vallance, 2009). These large lahars are not the only potential debris flow hazards. Mount Rainier also hosts smaller and much more frequent debris flows, which have damaged park infrastructure and led to the closure of public access to some of the park's road and trail infrastructure (Beason *et al.*, 2021).

Tahoma Creek (Fig. 1a), sits on the southwest side of Mount Rainier (Fig. 1b), is fed by glacial runoff from the Tahoma and South Tahoma Glaciers, and provides an excellent study site for debris flow processes on the mountain. Since 1926, there have been over 60 documented debris flows at Mount Rainier (Beason *et al.*, 2021). At least 33 of these debris flows have originated from the South Tahoma Glacier and flowed down Tahoma Creek (Walder and Driedger, 1995; Beason *et al.*, 2021). The South Tahoma Glacier feeds the main branch of Tahoma Creek. In its upper portions, Tahoma Creek is steep (25%–30% slope), narrow (10–30 m), and highly channelized (Fig. 1c), running through mostly fine sediment and hydrothermally altered clays at the glacial terminus. The South Tahoma Glacier has been retreating over the last half century,

Downloaded from pubs.geoscienceworld.org/ssa/srl/article-pdf/doi/10.1785/0220260021/8435001/srl-2026021.1.pdf by guest on 06 November 2026

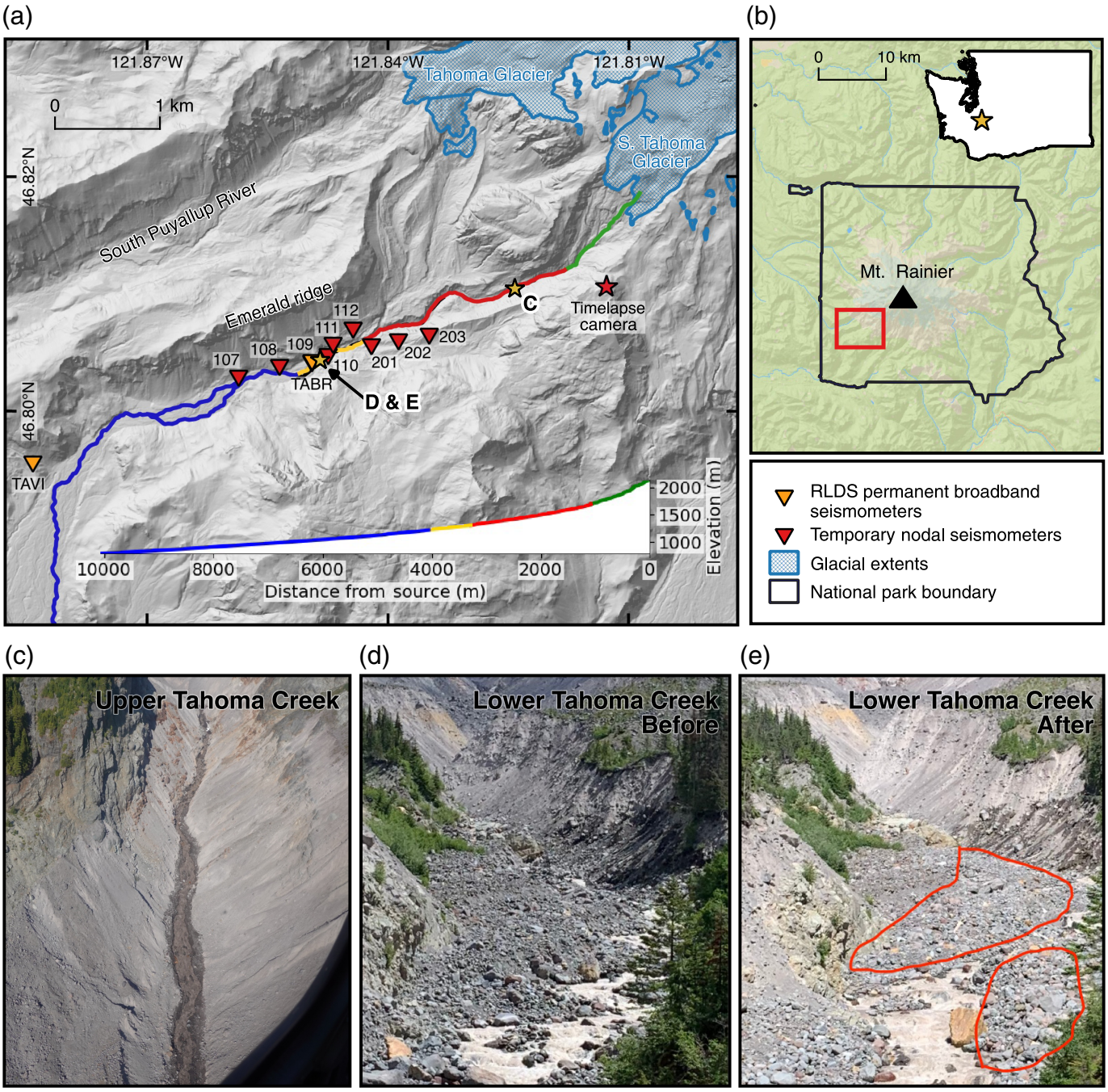


Figure 1. (a) Map of the Tahoma Creek drainage with the inferred path of the 2023 debris flow (colored line) and seismic stations (triangles) deployed along the channel. The flow path is color-coded by flow phase, with debris flow (initiation) in green, debris flow (transport) in red, debris flow (deposition) in yellow, and hyperconcentrated flow in blue. The inset diagram is the elevation profile of the flow path with 3× vertical exaggeration. Permanent stations that are a part of the Rainier Lahar Detection System (RLDS) are in orange. Temporary nodal seismometers are red. The stations TABR and 109 are collocated. Glacial extents are shown in light blue. Tahoma Creek is fed by both the Tahoma Glacier from the north Tahoma Creek branch and the South Tahoma Glacier from the main branch of Tahoma Creek, which is where this debris flow originated. The yellow stars show the location of the photos in (c–e). The red star shows the location of a time-lapse camera pointed at the glacier. Basemap credit (Washington Geological Survey, 2023). (b) Regional context showing the study area (red box) within the Mount Rainier National Park boundaries (black line) and the greater regional context of Mount Rainier National Park in the state of Washington, United States (inset). Basemap credit (Esri, 2016). (c) Aerial photo of Tahoma Creek taken high in the drainage showing steep channelization. Photo credit: Scott Beason, U.S. National Park Service. (d,e) Before and after photos of the transition zone at Tahoma Creek showing deposition that occurred as a result of the 2023 debris flow (red outlines). Photo credit: Weston Thelen, U.S. Geological Survey. The color version of this figure is available only in the electronic edition.

Downloaded from pubs.geoscienceworld.org/ssa/srl/article-pdf/doi/10.1785/0220260021/8435001/srl-2026021.1.pdf by guest on 06 November 2026

and debris flows are often linked to the glacial outburst events from this glacier, usually occurring on days with both hot and dry weather (Beason *et al.*, 2021). Debris flows in this channel have occurred most recently in 2019, 2023 (Iezzi *et al.*, 2024; Kramer *et al.*, 2024), and 2025. Approximately 2.5 km from the South Tahoma Glacier, another branch of the river, draining from the Tahoma Glacier, meets the main branch of Tahoma Creek from the north, and the slope begins to decrease, though the channel remains constricted by steep topography on both sides for another 200 m. At this point, the channel widens to 60 m wide and the slope decreases further to <10% (Fig. 1d,e), then transitions over the next 800 m into a wide braided riverbed channel. In this study, we will examine seismic data from this broad zone where the channel morphology changes.

In this article, we will be discussing a small debris flow that occurred in Tahoma Creek on 15 August 2023. This debris flow is classified as a dry debris flow (Beason *et al.*, 2021) because it occurred on a hot, dry day starting at approximately 4:24 p.m. local time (UTC23:24) with an outburst event on the South Tahoma Glacier face. The outburst event and rapid erosion and incision of material from the lower glacier face were observed by a time-lapse camera positioned to the south of the Tahoma Creek (Fig. 1a; images seen in Fig. S3, available in the supplemental material to this article). We have one laser rangefinder collocated with station TABR/109, which indicates a peak flow depth of 2 m at this location. Elevated flow from the glacier persisted for over 24 hr after the event. In this article, we present the seismic records of this event from a deployment of nodal seismometers, satellite imagery analysis of the flow path, and estimates of the amount of material deposited within the flow-path interval coinciding with the seismometer deployment.

Seismic data and analysis

The nine nodal seismometers used in this study were part of a larger nodal seismometer campaign (Fig. S1), deployed from 18 July 2023 to 24 August 2023 in and around the Tahoma Creek drainage in Mount Rainier National Park. We have chosen to highlight these 10 seismometers due to their close proximity to the river channel, creating the "near-field" seismic record of this event (Allstadt *et al.*, 2018). This nodal deployment has been part of an ongoing campaign to better understand debris flows at Mount Rainier as part of the Rainier Lahar Detection System (RLDS). In this study, we have included waveform data from TABR, a permanent broadband station in the RLDS, which is collocated with station 109 (Kramer *et al.*, 2024). The seismometers used in this deployment are three-component Fairfield Zland nodes with a 5 Hz corner frequency and a 500 Hz sampling rate. Although these nodes have a corner frequency of 5 Hz, they are capable of recording frequencies below 1 Hz (Ringler *et al.*, 2018). We do limit our analysis to >5 Hz. The nodal seismometers were installed every 100–200 m along the channel within 150 m of the channel laterally, where the channel is accessible. Some stations are farther apart due to steep terrain.

Because of this study location in a U.S. National Park, the study permit did not allow for the nodal seismometers to be buried. When unburied, Fairfield Zland nodes have a resonant noise frequency, depending on site-specific conditions and instrument installation method, that ranges from 10 to 100 Hz (Farrell *et al.*, 2018). Studies in the Tahoma Creek drainage have placed this frequency band locally from 25 to 41 Hz (Conner *et al.*, 2026), but weather conditions and air temperature can affect this frequency range (Farrell *et al.*, 2018). We calculated the center frequencies of the resonance bands by taking the maximum power spectral density (PSD) from waveform snippets representing regular flow before the debris flow event began, finding that the center frequencies range from 13.49 to 57.40 Hz. Each station in this study had a unique center frequency for resonance, and many stations had more than one pronounced resonance band.

Our goal with waveform processing was to remove the resonant noise and preserve the debris flow signal. Waveforms are detrended using both linear and mean detrending, and a taper is applied to smooth edge effects. To remove resonance, we apply second-order infinite-impulse-response adaptive notch filters at each station, a technique for removing sinusoidal noise, such as power grid signals, that vary around their average (Chicharo and Ng, 1990; Regalia, 1991; Bellanger, 2001). We apply these filters iteratively because the instrument resonance is a complex sinusoidal signal. Applying these filters iteratively slightly increases the notch width each iteration, removing additional signal with each iteration (Kelly *et al.*, 2016). Therefore, our initial filter passes are conservative, and we gradually increase the amount of both noise and signal removed with each filter pass. Details of the specific adaptive notch filters and signal processing for each station are provided in the supplemental material (Figs. S5–S13).

To calculate waveform envelopes, we apply a 1D Gaussian filter smoothing to the seismic envelope computed using the Hilbert transform. Spectrograms are calculated using the Pywavelet continuous wavelet transform (CWT) function (Torrence and Compo, 1998; Lee *et al.*, 2019). The CWT is performed using a complex Morlet wavelet with a bandwidth of 50 and a center frequency of 1 Hz. Spectrograms are presented on a log-normalized scale to indicate power in decibels. All spectrograms are presented on the same decibel scale (10^{-14} to 10^{-8} dB). We calculate PSD using the method of Welch (1967) for rolling 60 s windows with 50% overlap. Peak frequencies are calculated from the maximum of the smoothed PSD using the method of Lai *et al.* (2018). In this case, the smoothed PSD is computed by convolving the PSD with a 120-sample moving-average filter, which is equivalent to a 2 Hz smoothing window. We also calculate the weighted mean frequency content of the PSD using the trapezoidal method because we observe multiple PSD peaks at some stations that may bias the peak frequency.

In addition, we estimated the average flow velocity between stations by cross-correlating the waveform envelopes. We cross-correlate waveform windows centered on the first distinct flow

Downloaded from pubs.geoscienceworld.org/ssa/srl/article-pdf/doi/10.1785/0220260021/8435001/srl-2026021.1.pdf by guest on 06 November 2026

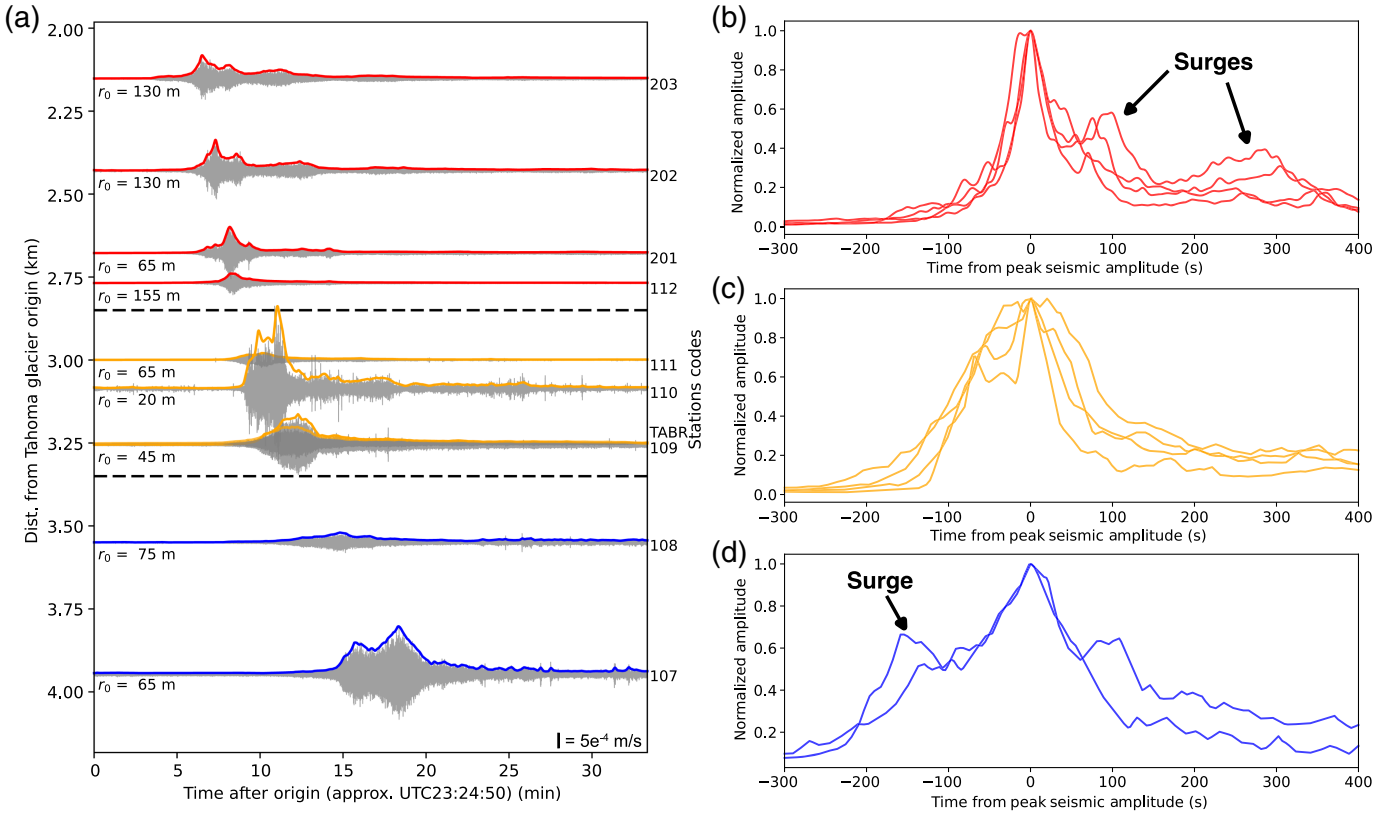


Figure 2. (a) Vertical-component waveforms sorted by distance from the source, with associated envelopes—red indicates debris flow (transport), yellow indicates debris flow (deposition), and blue indicates hyperconcentrated flow. The approximate locations of the transitions between the flow stages are shown using dashed black lines. The r_0 values indicate the distance between the station and the flow path. A comparison of stations 109 and TABR, which overlap, can be found in Figure S4. (b–d) Windowed and normalized envelopes aligned by peak amplitude for (b) debris flow (transport) envelopes at stations 203, 202, 201, and 112, (c) debris flow (deposition) envelopes at stations 111, 110, 109, and TABR, and (d) hyperconcentrated flow envelopes at stations 108 and 107. The color version of this figure is available only in the electronic edition.

surge to find the time delay between stations. We divide the distance the flow traveled downstream between stations by the time lag to find the average velocity between neighboring station pairs. Because of the characteristics of the event, the first distinct peak in the waveform corresponds to the highest amplitude recorded from the event at all stations except 107 (Fig. 2a,d). To account for the discrepancy, we additionally find the lag time between the peak amplitude at stations 108 and 107 by cross-correlating the envelope of the entire event waveform at each station, and estimate a second velocity from the results. Velocity estimates between station pairs are presented in Table S1.

Digital elevation model differencing and imagery analysis

We additionally characterized the event path, flow-type, and volume using a combination of high-resolution optical satellite imagery, aerial reconnaissance photos collected by helicopter on 15 August 2023 within two hours of the debris flow, and field photos collected before (11 July 2023) and after the event (9 July 2024) from a bridge overlooking the main area of deposition. High-resolution imagery analyzed includes postevent Worldview 2 (WV02) satellite imagery captured on 18 August 2023 and post-event imagery from 03 July 2024 accessed in Google Earth, compared against pre-event WV02 imagery captured on 28 June 2023 (Fig. S2). In addition to this imagery, we also created a post-event digital surface model (DSM), using a 14 July 2024 WV02 stereo image pair and surface extraction by triangulated-irregular-network-based Search Space Minimization (SETSM) software (Noh and Howat, 2017). This postevent DSM was aligned and then differenced from a pre-event light detection and ranging (LiDAR) digital terrain model (DTM; Washington Geological Survey, 2023) to create a digital elevation model (DEM) difference product. We aligned the pre- and postevent elevation models in CloudCompare (CloudCompare (version 2.12.2) [GPL software], 2024), a 3D point-cloud processing software, using tree-free stable regions on either side of the channel and adjacent slopes. Both elevation models are sampled at a 2-m resolution and projected to the same coordinate reference system (EPSG:32610, UTM zone 10N). Areas of tree cover and shadows were excluded from analysis. Our estimate of the minimum resolution for the detection of elevation changes is 0.8 m. This is the standard deviation

Downloaded from pubs.geoscienceworld.org/ssa/srl/article-pdf/doi/10.1785/0220260021/8435001/srl-2026021.1.pdf by guest on 06 November 2026

of differences between the pre- and postevent elevation models in tree-free areas in the vicinity of the deposits that we assumed should be stable based on context.

We digitized the approximate flow path using the satellite imagery and pre-event lidar DTM. We calculated the average slope angles along the flow path by sampling pre-event DTM elevations every 2 m along the path, computing slope, and then smoothing along this profile line using a Gaussian kernel with a standard deviation of 200 m. All distances from the source reported in this article were computed along the same flow path. The flow path was parsed into different sections based on the following flow-type classifications: (1) the initial outburst flood, (2) debris flow initiation (erosion dominant, steep slopes), (3) debris flow transport (a mix of erosion and deposition, but primarily travel), (4) debris flow deposition (primarily deposition), and (5) hyperconcentrated flow (termination of debris flow deposits), which were determined by field and aerial reconnaissance photos and the DEM difference product. The initial outburst flood was also captured by a time-lapse camera facing the glacier (Fig. S3).

We used the imagery and DEM difference product to delineate areas of erosion and deposition. When possible, negative and positive elevation changes seen in the DEM difference were verified, augmented, and refined using the field and/or aerial reconnaissance photographs. Verification was critical to ensure we were not capturing elevation changes unrelated to the 15 August 2023 debris flow, given that the postevent DSM is from 11 months after the debris flow and also contains substantial noise. We estimated the volume of the main debris flow deposits by integrating the positive elevation differences in the areas we delineated as deposits along the section of the path classified as debris flow deposition. We estimated volume uncertainty using the standard deviation from CloudCompare's multiscale model-to-model cloud comparison (M3C2; Lauge *et al.*, 2013) in stable regions used for alignment and a spatial correlation distance estimated using methods of Allstadt *et al.* (2024). The standard deviation of the vertical difference in elevation in the vicinity of the deposits was 0.8 m, and the distance over which the errors were correlated was 67 m. The standard deviation of vertical difference in elevation in the entire DEM difference region, using the alignment of stable rock outcrops, was 2.7 m. Finally, we used the QGIS measuring tool on the satellite imagery to obtain a rough estimate of the size of the largest deposited boulders observed in the satellite imagery. The DEM difference product, postevent DSM, flow path, and volume polygons are available from Collins *et al.* (2026).

Results

Seismic waveforms and envelopes

As the 15 August 2023 flow traveled down the Tahoma Creek channel, it was recorded by the 10 along-channel seismometers located 2–4 km downstream from the outburst source at South Tahoma Glacier. The vertical-component seismograms and their smoothed envelopes are shown in Figure 2a. Flow-event seismic signals on each station persist for tens of minutes, and amplitudes may wax and wane multiple times, reflecting distinct phases of flow activity or successive surges. Because these stations are effectively in the near field (<155 m), the dominant seismic energy arises from the portion of the debris flow closest to each station, although other parts of the flow also contribute to the signal (Allstadt *et al.*, 2018). In this event, the waveform envelopes (Fig. 2b–d) show that the signal progressively elongates downstream and that the peak amplitude has a longer delay relative to signal onset as the flow advances. When the peak amplitude occurs at the onset of the signal, as in Figure 2b, it indicates the presence of a characteristic debris flow snout, a feature of debris flow sorting where larger material collects at the front of the flow body (Hsu *et al.*, 2011; Farin *et al.*, 2019). Multiple subsequent surges are clearly expressed in the envelopes following the snout and produce secondary amplitude peaks. These surges are less distinct during the transition stage (Fig. 2c). Farther downstream, the largest amplitude no longer corresponds to the first surge (Fig. 2d); instead, the initial surges have smaller amplitudes, and the maximum amplitude is reached later in the signal.

In the upper portion of the channel, above station 112, the estimated flow velocity between stations is >5.8 m/s, with a maximum value of 6.8 m/s between stations 201 and 112. Below station 112, flow velocities are less than half of the flow velocity in the upper channel (<2.9 m/s), with the estimated minimum flow velocity (2.1 m/s) occurring between stations 111 and 110. At the end of our monitoring coverage, the flow has effectively formed two large waves, with the preceding surge being smaller in amplitude than the secondary surge. In this case, we calculated the velocity between station 108 and both the first and second surges at station 107, which are 4.5 and 1.9 m/s, respectively. A table of the flow velocities between station intervals can be found in Table S1.

Spectral analysis

To further analyze the signal frequency content, we present spectrograms for the three flow stages (Fig. 3a,c,e), where we show the 5–250 Hz spectrograms for stations 201, 111, and 107, each representative of the three different stages of flow behavior we observe. Similar spectrograms for all stations are shown in the supplemental material (Figs. S5–S13). These representative stations were chosen because they are equidistant from the channel. We show the total seismic PSD for all stations in this study in Figure 3b,d,f, classified by the flow stage at each station. We note that site effects are likely highly varied along the channel (Conner *et al.*, 2026), and that changes from one station to another are partially dependent on these effects. Grouping the seismic PSDs by flow classification (Fig. 3b,d,f) does show consistent spectral changes across the flow type classifications.

Downloaded from pubs.geoscienceworld.org/ssa/srl/article-pdf/doi/10.1785/0220260021/8435001/srl-2026021.1.pdf by guest on 06 November 2026

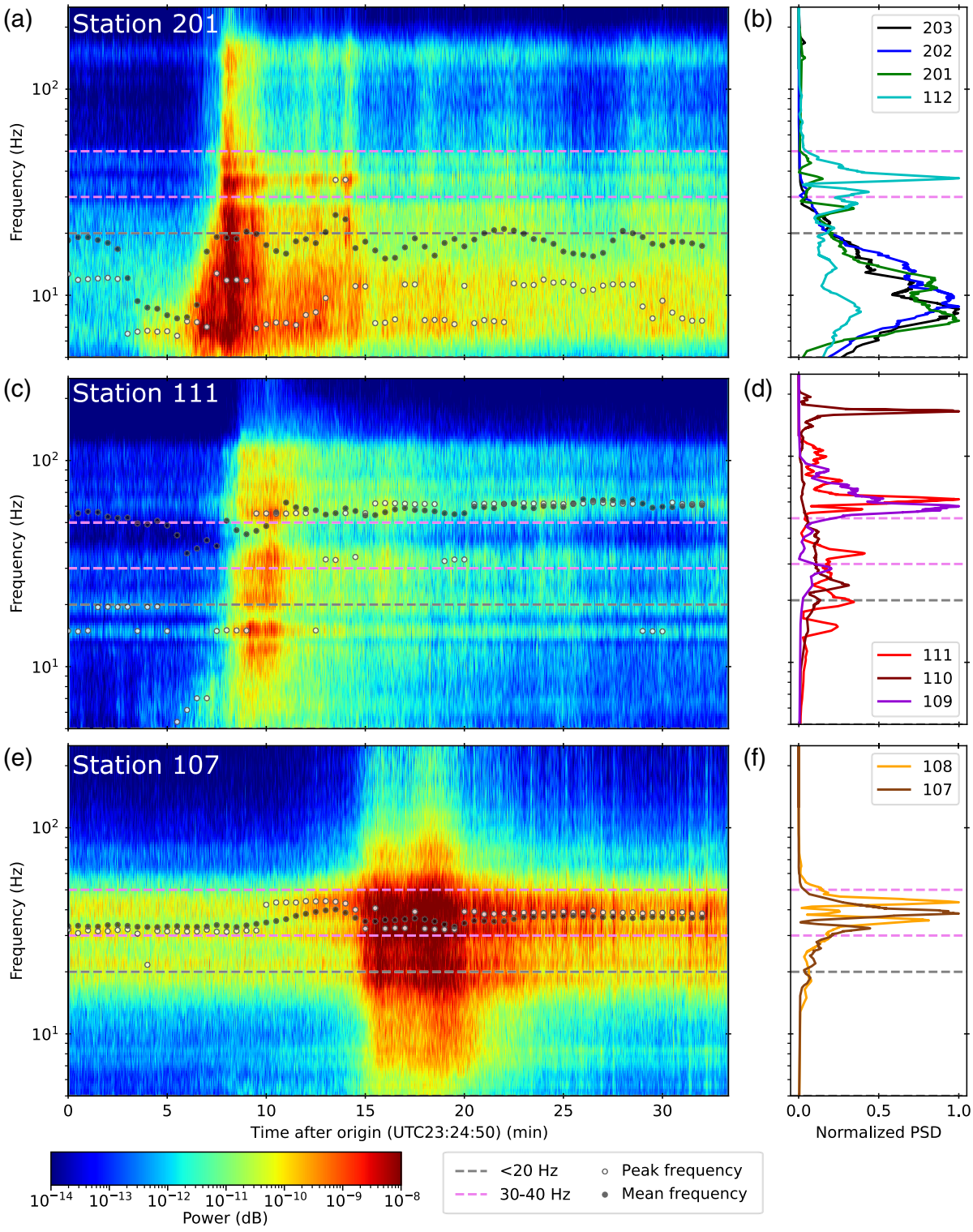


Figure 3. (a,c,e) Filtered continuous wavelet transform (CWT) spectrograms for frequencies from 5 to 250 Hz for stations (a) 201—upper channel, debris flow (transport) stage, (c) 111—transition zone, debris flow (deposition) stage, and (e) 107—lower channel, hyperconcentrated flow stage. Peak frequencies for 60 s smoothed overlapping windows of the power spectral density (PSD) of the signals are shown in white. The mean frequency content of the windowed PSDs is shown in black. All three stations are the same distance of 65 m from the channel. The gray dashed lines show the frequency interval from <20 Hz, and the pink dashed lines show the frequency interval from 30 to 40 Hz. (b,d, f) Normalized total PSD for the entire waveform window for all stations classified by (b) debris flow (transport), (d) debris flow (deposition), and (f) hyperconcentrated flow. The <20 Hz (gray) and 30–40 Hz (pink) bands are indicated by the dashed lines. The color version of this figure is available only in the electronic edition.

Downloaded from pubs.geoscienceworld.org/ssa/srl/article-pdf/doi/10.1785/0220260021/8435001/srl-2026021.1.pdf by guest on 06 November 2026

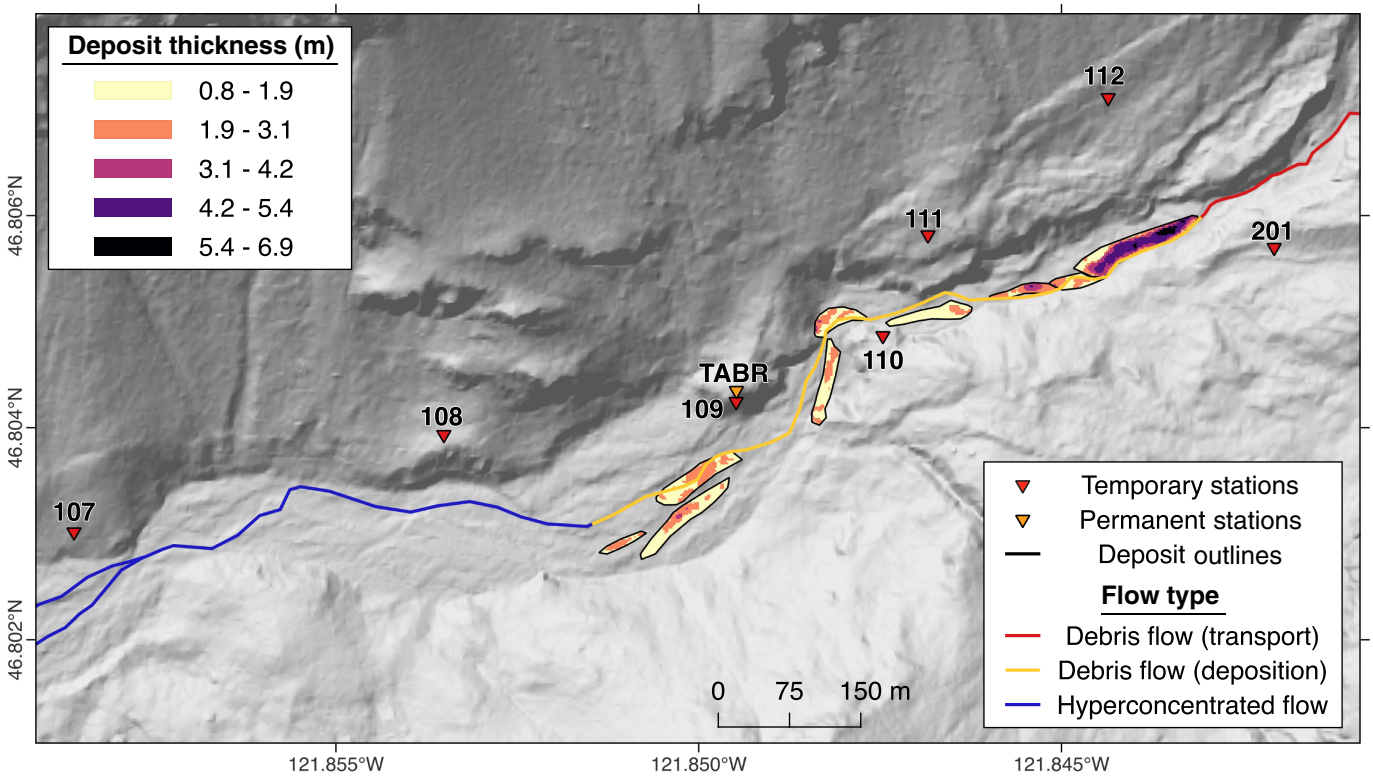


Figure 4. Map showing mapped zones of deposition (black outlines) with thickness ranging from 0.8 to 6.9 m over the zone of debris flow deposition (yellow dashed line) occurring between stations 201 and 108. Tahoma Creek flows east (right) to west (left) in this image. Basemap credit (Washington Geological Survey, 2023). The color version of this figure is available only in the electronic edition.

The spectrograms show a stark change in the signal over the course of the flow. Station 201 (Fig. 3a) shows a low-frequency signal onset until we observe the suspected snout arrival at approximately 7 min. Here, we observe the event's maximum peak frequency (11 Hz) and the broadest frequency content (5–50 Hz). After the peak seismic energy, the peak frequency decreases, remaining below 10 Hz, and the signal's frequency range narrows. The largest amount of seismic energy for stations in the debris flow transport stage of flow falls in the 5–20 Hz range (gray lines in Fig. 3b). Station 112, located upstream from the start of the depositional zone where the river channel widens, records seismic power in the 5–20 Hz band, but also has a spike in power at the 30–40 Hz band. Because of its proximity to the depositional zone, this station may be recording this transition to depositional processes.

Station 111 (Fig. 3c), which is in the depositional zone, shows a low-power, low-frequency onset at approximately 7.5–8 min. There is a strong broad-frequency arrival directly after this, which tapers off quickly within a few minutes. Peak frequency is difficult to determine at this station and at other stations in this section, as all stations exhibit multiple resonance bands that are difficult to remove completely without compromising the underlying signal, which is related to site-specific conditions. It should be noted that the peak in PSD during this interval, between stations 111 and 109, is higher (>40 Hz) than at any other time in the flow (Fig. 3d).

At station 107 (Fig. 3e), there is broad noise from 20 to 50 Hz in the background of the signal. The spectrogram shows no low-frequency onset. The main signal lasts from 15 to 20 min with a broad frequency signal from 5 to 100 Hz, and the strongest signal is in the 20–50 Hz range. The signal slowly tapers after 20 min, but remains elevated relative to the initial signal level. Peak frequencies during the strongest part of the signal are around 32 Hz. Stations 108 and 107 are located downstream from the main deposition interval and have seismic energy falling mostly in the 30–40 Hz interval (pink lines in Fig. 3f).

Along channel deposits

DEM differencing and imagery analysis reveal that the main debris flow deposits (Fig. 4) are located in a transition zone between stations 201 and 108, where the channel transitions from a narrow, steep (25%–10% slope) canyon to a wider, less steep, and curvilinear (10%–11% slope) channel section. The length of the deposition zone is ~800 m, or <8% of the total debris flow runout length, which is >9.9 km. In optical WV02 imagery from 18 August 2023, deposits appear lighter in color compared to the surrounding material, potentially due to a coating of mud, but are generally similar in geologic composition and grain size distribution to material deposited from previous flows in this section of Tahoma Creek. The major-axis

Downloaded from pubs.geoscienceworld.org/ssa/srl/article-pdf/doi/10.1785/0220260021/8435001/srl-2026021.1.pdf by guest on 06 November 2026

length of boulders in the deposits roughly ranged from ~0.8 to 3.6 m, and deposit thicknesses ranged between 0.8 and 6.9 m. We identified nine separate deposits in this region (Fig. 4)—three between stations 111 and 201, one between 110 and 111, two between 109/TABR and 110, and three between 108 and 109/TABR. The total volume of the deposits, in the debris flow deposition zone, was 24,000 ± 4800 m^3. Note that there were smaller areas of additional deposition upstream and downstream that are not included in this total. About 73% of the total volume was deposited above stations 109 and TABR, with 54.2% of the total volume deposited in the first region after the flow exits the narrow, steep canyon, between stations 111 and 201.

Discussion

Three distinct flow stages based on waveforms: Debris flow, deposition, and hyperconcentrated flow

The seismic data recorded during this debris flow event allow us to study the seismic evolution of a debris flow through the process of sediment deposition. During the debris flow transport (Figs. 2b and 3a,b) stage, the flow has a distinct debris flow snout, multiple following surges, and remarkably minimal signal changes in shape and power between the stations in the upper channel (203, 202, 201, and 112), which are hundreds of meters apart. The earliest signal from the debris flow emerges from the background signal at low frequencies below 10 Hz, with a gradual crescendo, as the leading edge of the upstream debris flow approaches the station. We interpret the arrival across a broad range of frequencies as the arrival of the debris flow snout at the closest part of the channel to the station. Peak frequencies are generally 5 Hz before this arrival, with a spike in peak frequency to about 11 Hz aligned with the snout arrival at 8 min (Fig. 3a), which is consistent with a decreasing source-to-receiver distance (Lai *et al.*, 2018; Wenner *et al.*, 2019; Belli *et al.*, 2022). The strongest energy occurs at this arrival (Walter *et al.*, 2017; Coviello *et al.*, 2019; Farin *et al.*, 2019; Belli *et al.*, 2025) and indicates that the snout has a broad spectral range. After the snout arrival, seismic signal peaks associated with subsequent surges have both lower power relative to the initial snout and narrower frequency spectra. Because the debris flow snout tends to contain the largest particles in the flow (Takahashi, 2014), the increased power relative to the rest of the flow indicates that the low-frequency noise in this seismic signal is linked to the impacts and shear stress of larger particles (Yang *et al.*, 2024; Márquez-Ramirez *et al.*, 2025). Finally, after the snout has moved past the station, the power in the lower frequencies gradually recedes, and the peak frequency gradually increases from 7.5 to 10 Hz, indicating that the particle diameters in later portions of the flow may be smaller than in the snout (Huang *et al.*, 2007; Burtin *et al.*, 2009) and that reduced flow height and sediment concentration may increase flow turbulence (Gimbert *et al.*, 2014; Belli *et al.*, 2025; Márquez-Ramirez *et al.*, 2025).

The debris flow deposition stage exhibits markedly different characteristics from the transport stage and a lower energy flow overall, as flow velocity has decreased due to geomorphological changes (Table S1). The signal is largely broadband, including high-frequency signal above 50 Hz, with peak frequency varying throughout the signal, complicated by the broad signal in the 20–50 Hz range consistent with river or sediment transport noise (Fig. 3c). Mean frequency, which is less biased by minor peaks in the frequency spectra, is above 30 Hz for the entire debris flow signal and above 40 Hz after the peak amplitude of the signal has passed. Most notably, all three nodal seismometers in this region—111, 110, and 109 (Fig. 3d)—have signal energy peaks from 40 Hz to above 100 Hz. Because this region is the zone of deposition, as indicated by the mapped deposits (Fig. 4), this high-frequency energy is likely a behavior of material deposition, possibly related to increased particle interactions due to the rough bed surface created by repeated deposition. Previous studies have noted that less-dense ground, as in this case where the flow moves over large areas of existing depositional layers over the bedrock, widens the frequency range of the associated debris flow signal (Huang *et al.*, 2007). Much like stations higher in the channel, stations in the debris flow deposition zone continue to show the low-frequency signal onset at <10 Hz, characteristic of the preceding increase in flow in the upper channel, although at a lower amplitude than stations higher in the channel.

By the time the flow arrives at the hyperconcentrated flow stage lower in the channel at station 108 (Fig. 3e), a considerable amount of material larger than gravel size has been deposited (~24,000 cubic meters), likely causing particles larger than gravel-sized particles to fall out of suspension in the flow (Beverage and Culbertson, 1964; Pierson and Scott, 1985; Pierson, 2005). In addition, the flow velocity has slowed to <2.6 m/s as the flow loses energy. The loss of this material, decreased sediment concentration, and reduced flow discharge appear to be reflected in the signal below 20 Hz, where low-frequency energy is reduced (Fig. 3e,f). The peak frequency has increased to approximately 30–40 Hz for the main signal. Both in time and in peak frequency, the signal no longer exhibits a substantial snout arrival expected for a debris flow; instead, we observe multiple longer pulses as the main body of the flow arrives, with the largest occurring later in the flow, nearly 20 min after initiation. The diffuse nature of the signal in these later stages and the lack of traceable features from station 108 to 107 indicate that the flow is affected by channel conditions, where surges form through progressive instabilities that grow over time (Zanuttigh and Lamberti 2007). Finally, the frequency content has shifted noticeably higher compared to the debris flow stages, with peak frequencies changing from below 10 Hz for the debris flow signals to 30–40 Hz for the hyperconcentrated flow signals, reflecting changes in material composition, sediment concentration, flow parameters such as height, and dynamics of the two flow stages between laminar debris

Downloaded from pubs.geoscienceworld.org/ssa/srl/article-pdf/doi/10.1785/0220260021/8435001/srl-2026021.1.pdf by guest on 06 November 2026

flow and turbulent hyperconcentrated flow (Gimbert *et al.*, 2014; de Haas *et al.*, 2021; Yang *et al.*, 2024; Márquez-Ramirez *et al.*, 2025).

The stations downstream from station 201 (Fig. 1a) have an elevated background signal in the 20–50 Hz range, indicating elevated sediment transport, water flow, and turbulence during baseline river flow (Burtin *et al.*, 2009; Schmandt *et al.*, 2013; Gimbert *et al.*, 2014; Belli *et al.*, 2025). This elevated signal is likely partially associated with elevated sediment load and water flow in the north fork of Tahoma Creek, which is closer to some of these stations than the main fork where the debris flow occurred. This second fork flows out of Tahoma Glacier. Both forks of Tahoma Creek have their highest seasonal flow in the late summer, driven by hot temperatures and elevated melt rates at the Tahoma and South Tahoma Glaciers (Beason *et al.*, 2021). This elevated flow includes increased transport during large mass events, such as this debris flow, which tend to be the largest mass transport events in Tahoma Creek.

Waveform transition occurs where expected geomorphologically

Over the analyzed stretch of channel between stations 203 and 107, the seismic signals associated with this debris flow clearly undergo considerable changes from start to finish, but the exact points of these changes occur between stations 112 and 111 and stations 109 and 108. The geomorphological changes in this portion of the channel, which include the changes in slope from 25% to <10%, a change in nonvegetated channel width from 10 ± 1 to 48 ± 4 m, and a change from a straight to curvilinear channel, would signify that a change in energy and flow velocity (Table S1) occurs quickly at the mouth of upper Tahoma Creek. Photos of this region (Fig. 1d,e) indicate that the channel is full of deposited material, including deposits from past debris flows. These morphological changes coincide with a flow state change, which occurs over just 20% of the total runout length of the debris flow (800 m of channel). As hyperconcentrated flows and debris flows exist on a continuum, it is difficult to say precisely in this region where the flow crosses the 60% threshold of sediment by volume (Pierson, 2005). Nevertheless, our findings indicate that this flow state change has occurred by the flow's arrival at station 108 (Fig. S12), where the flow's seismic signal has notably lost low-frequency energy and shows a changed envelope shape more consistent with a snoutless structure relative to flow signals upstream from station 112.

Grain size and sediment concentration change the frequency content of the flow signal

Perhaps the most notable conclusion of this study is that the particle-size distribution and sediment concentration of the flow event may alter the frequency content of the flow signal, which changes as a function of time and distance as the flow progresses downstream. Previous studies have suggested a potential relationship between particle size, sediment concentration, and signal frequency, indicating that collisions of larger boulders in debris flow channels are associated with relatively lower frequencies than those of smaller boulders (Huang *et al.*, 2007; Burtin *et al.*, 2009; Yang *et al.*, 2024; Márquez-Ramirez *et al.*, 2025). Larger material in the debris flow transport zone of this event, including boulders up to 3.6 m in diameter, is mainly observed along the parts of the channel before the geomorphological change where seismic signals have substantial frequency content below 20 Hz. By the time the flow passes seismic stations along the lower stretches of the channel, 24,000 cubic meters of material have been deposited, including the largest diameter material, and the signal has shifted 20 Hz higher in frequency, with little to no signal below 20 Hz. These changes are consistent with a loss of larger material from the flow, the lowering of sediment concentration, and the overall loss of energy due to changes in the flow velocity and total discharge as a result the geomorphological changes.

That material size changes signal frequency composition is not unexpected; however, physical models of debris flow seismic signals do present a simplified model of these flow events and, consequently, do not account for these frequency variations. Both Farin *et al.* (2019) and Lai *et al.* (2018), for example, propose that particle diameter affects total spectral power, but not frequency. The Farin *et al.* (2019) model has been validated for laboratory-scale experiments (Arran *et al.*, 2021). Notably, both models consider debris flows over bedrock and do not account for a deformable bed, one major caveat in this instance.

The underlying physical assumptions of these debris flow models are based on the Tsai *et al.* (2012) sediment transport model, which shows that particle diameter affects total power over a range of frequencies, but the peak frequency remains unchanged as particle diameter changes. However, we found a shift in peak frequency as material settles out of transport and sediment concentration decreases, although these occur alongside additional flow changes like decreases in velocity and likely flow depth. Shifts in peak frequency over the course of a debris flow were noted in Lai *et al.* (2018), but the authors hypothesized that the observed shift of the peak frequency by 5 Hz as the flow passed the station was due solely to the flow moving away from the station, not flow composition changes. We observe a similar phenomenon in Figure 3a, with an increase in peak frequency following the snout arrival. Although we note that at greater distances, the flow noise is likely coming from the body or the flow's extended tail, this gradual increase in frequency likely reflects smaller particle sizes and total discharge in the flow's tail versus its surge front (Burtin *et al.*, 2009).

For future consideration in physical modeling of debris flow, we propose two considerations: (1) Particle collisions with the bed of the channel may not be an instantaneous, elastic impact. This is particularly true in channels with existing sediment cover, which may dampen and prolong these

Downloaded from pubs.geoscienceworld.org/ssa/srl/article-pdf/doi/10.1785/0220260021/8435001/srl-2026021.1.pdf by guest on 06 November 2026

collisions. (2) The bedrock assumption also influences the frequency content of the signals. We observe this particularly during the channel-deposition section, where a high-frequency signal appears to correspond to thick layers of sediment deposited in the channel during this and previous debris flows.

Conclusion

In this article, we present and analyze seismic recordings and remote-sensing observations of a debris flow triggered by a glacial outburst at Tahoma Creek in Mount Rainier National Park. The along-channel nodal array captured systematic changes in waveform character that coincide with a major geomorphic transition 2.5 km downstream from the source, where the channel widens substantially and the slope decreases from 25% to 10%. Over ~800 m, the signal progressively loses the rapid onset-to-peak amplitude characteristic of a well-defined debris flow snout, and the dominant frequency band shifts from 5–20 to 30–40 Hz. These seismic changes occur contemporaneously with the deposition of approximately 24,000 m^3 of material across nine mapped deposits, including boulders up to 3.6 m in diameter.

We interpret the observed waveform and frequency changes as marking the transition from debris flow to hyperconcentrated flow, during which sediment concentrations fall below ~60% by volume, and the flow loses its internal sorting and coherent snout structure. The downstream loss of energy below 20 Hz indicates that the lowest-frequency components of the signal are associated with the transport and interaction of large clasts and elevated sediment concentration. Characterizing this transition and its seismic expression has important implications for hazard assessment because flow type directly influences runout potential, total discharge, and damage potential. Moreover, the potential link we observe between particle size, sediment concentration, and seismic frequency content indicates that debris flow seismic models can be improved by explicitly incorporating grain-size-dependent signal generation and relaxing bedrock and instantaneous-collision assumptions to reproduce the full range of field observations.

Data and Resources

Seismic data used in this study were accessed through the EarthScope Consortium web services (https://service.iris.edu/, last accessed October 2026), from the assorted network codes that include "4K" for the 2023 Mt. Rainier Deployment (University of Oregon, 2023), "CC" for the Cascade Chain Volcanic Monitoring Network (Cascades Volcano Observatory [CVO], 2023), and "UW" for the Pacific Northwest Seismic Network (University of Washington, 2023). Software used to analyze the seismic signals includes ObsPy (Beyreuther *et al.*, 2010) and the Pywavelet continuous wavelet transform (CWT; Torrence and Compo, 1998; Lee *et al.*, 2019). Imagery and aerial photo processing used the Washington Geological Survey light detection and ranging (LiDAR) digital elevation model (DEM) of Mount Rainier (Washington Geological Survey, 2023) as well as Worldview 2 (WV02) satellite imagery, which was accessed via license from Maxar (2023, Maxar, USG Plus). DEM processing was done using the SETSM software (Noh and Howat, 2017) and CloudCompare (CloudCompare (version 2.12.2) [GPL software], 2024). The debris flow path and depositional volumes were released in Collins *et al.* (2026). Figures were produced in QGIS (QGIS.org, 2024) using the Washington Geological Survey DEM for the local basemap (Washington Geological Survey, 2023) or the ESRI Oceans Basemap (Esri, 2016) for larger regional maps. The supplemental material for this article includes additional figures showing the full nodal seismic deployment, satellite imagery processing, changes to the glacial face recorded by the time-lapse camera, comparing the collocated stations 109 and TABR, and a detailed breakdown of the filtering process for the nodal stations 203, 202, 201, 112, 111, 110, 109, 108, and 107.

Declaration of Competing Interests

The authors acknowledge that there are no conflicts of interest recorded.

Acknowledgments

This work was supported by the U.S. Geological Survey (USGS) through Cooperative Agreement Number G23AC00557 as part of the Rainier Lahar Detection System (RLDS) project. The authors thank Lucia Capra and Giancomo Belli for their thorough and valuable input in reviewing this article.

Any use of trade, firm, or product names is for descriptive purposes only and does not imply endorsement by the U.S. Government.

References

Allstadt, K. E., J. A. Coe, E. A. Collins, F. K. Rengers, A. Mangeney, S. M. Esser, J. Pursley, W. L. Yeck, J. J. Bellini, and L. R. Brady (2024). The 2022 Chaos Canyon landslide in Colorado: Insights revealed by seismic analysis, field investigations, and remote sensing, *Landslides* **21,** 309–325, doi: 10.1007/s10346-023-02179-4.

Allstadt, K. E., R. S. Matoza, A. B. Lockhart, S. C. Moran, J. Caplan-Auerbach, M. M. Haney, W. A. Thelen, and S. D. Malone (2018). Seismic and acoustic signatures of surficial mass movements at volcanoes, *J. Volcanol. Geotherm. Res.* **364,** 76–106, doi: 10.1016/j.jvolgeores.2018.09.007.

Andrade, S. D., S. Almeida, E. Saltos, D. Pacheco, S. Hernandex, and W. Acero (2022). A simple and general methodology to calibrate seismic instruments for debris flow quantification: application to Cotopaxi and Tungurahua volcanoes (Ecuador), *Landslides* **19,** 747–759, doi: 10.1007/s10346-021-01784-5.

Arran, M. I., A. Mangeney, J. De Rosny, M. Farin, R. Toussaint, and O. Roche (2021). Laboratory landquakes: Insights from experiments into the high-frequency seismic signal generated by geophysical granular flows, *J. Geophys. Res. Earth Surf.* **126,** no. 5, e2021JF006172, doi: 10.1029/2021JF006172.

Beason, S. R., N. T. Legg, T. R. Kenyon, and R. P. Jost (2021). Forecasting and seismic detection of proglacial debris flows at Mount Rainier National Park, Washington, USA, *Environ. Eng. Geosci.* **27,** no. 1, 57–72, doi: 10.2113/EEG-D-20-00014.

Bellanger, M. (2001). *Adaptive Digital Filters*, Marcel Dekker, Inc., New York, NY, USA.

Belli, G., E. Marchetti, F. Walter, and D. Gheri (2025). Infrasound unmasks flow turbulence as an additional seismic source in debris

Downloaded from pubs.geoscienceworld.org/ssa/srl/article-pdf/doi/10.1785/0220260021/8435001/srl-2026021.1.pdf by guest on 06 November 2026

flows, *Geophys. Res. Lett.* **52,** no. 8, e2025GL116107, doi: 10.1029/2025GL116107.

Belli, G., L. Marchi, M. Piantini, G. Nagl, and P. Macconi (2026). Investigating the relationship between seismic and infrasonic source mechanisms in debris flows, *Landslides* **23,** 2049–2061, doi: 10.1007/s10346-026-02727-8.

Belli, G., F. Walter, B. McArdell, D. Gheri, and E. Marchetti (2022). Infrasonic and seismic analysis of debris-flow events at Illgraben (Switzerland): Relating signal features to flow parameters and to the seismo-acoustic source mechanism, *J. Geophys. Res. Earth Surf.* **127,** no. 6, e2021JF006576, doi: 10.1029/2021JF006576.

Beverage, J. P., and J. K. Culbertson (1964). Hyperconcentrations of suspended sediment, *J. Hydraul. Div.* **90,** 117–128, doi: 10.1061/JYCEAJ.0001128.

Beyreuther, M., R. Barsch, L. Krischer, T. Megies, Y. Behr, and J. Wassermann (2010). ObsPy: A Python toolbox for seismology, *Seismol. Res. Lett.* **81,** no. 3, 530–533, doi: 10.1785/gssrl.81.3.530.

Burtin, A., L. Bollinger, R. Cattin, J. Vergne, and J. L. Nábělek (2009). Spatiotemporal sequence of Himalayan debris flow from analysis of high–frequency seismic noise, *J. Geophys. Res. Earth Surf.* **114,** no. F4, doi: 10.1029/2008JF001198.

Cascades Volcano Observatory (CVO) (2023). Cascade chain volcano monitoring, doi: 10.7914/SN/CC.

Cavagnaro, D. B., S. W. McCoy, J. W. Kean, M. A. Thomas, D. N. Lindsay, B. W. McArdell, and J. Hirschberg (2024). A robust quantitative method to distinguish runoff-generated debris flows from floods, *Geophys. Res. Lett.* **51,** no. 15, e2024GL109768, doi: 10.1029/2024GL109768.

Chicharo, J., and T. Ng (1990). Gradient-based adaptive iir notch filtering for frequency estimation, *IEEE Trans. Acoust. Speech Signal Process.* **38,** no. 5, 769–777, doi: 10.1109/29.56021.

CloudCompare (version 2.13.2) [GPL software] (2024). CloudCompare, available at https://www.cloudcompare.org/ (last accessed October 2026).

Cole, S. E., S. J. Cronin, S. Sherburn, and V. Manville (2009). Seismic signals of snow-slurry lahars in motion: 25 September 2007, Mt Ruapehu, New Zealand, *Geophys. Res. Lett.* **36,** doi: 10.1029/2009GL038030.

Collins, E., K. Allstadt, and S. Beason (2026). Elevation difference products, schematic flow path, and volume polygons for the 15 august 2023 debris flow in Tahoma Creek, Mount Rainier, doi: 10.5066/P13VEXJM.

Conner, A. E., A. M. Thomas, K. E. Allstadt, W. A. Thelen, E. Collins, M. Farin, W. J. Stephenson, A. M. Iezzi, and K. M. Biegel (2026). Quantifying seismic properties of a river channel at Mount Rainier for use in debris flow monitoring and analysis, *Seismol. Res. Lett.* doi: 10.1785/0220250071.

Coviello, V., M. Arattano, F. Comiti, P. Macconi, and L. Marchi (2019). Seismic characterization of debris flows: Insights into energy radiation and implications for warning, *J. Geophys. Res. Earth Surf.* **124,** 1440–1463, doi: 10.1029/2018JF004683.

Crandell, D. R. (1971). Postglacial lahars from Mount Rainier volcano, Washington, *U.S. Geol. Surv. Professional Paper 677*.

de Haas, T., A. S. Åberg, F. Walter, and Z. Zhang (2021). Deciphering seismic and normal-force fluctuation signatures of debris flows: An experimental assessment of effects of flow composition and dynamics, *Earth Surf. Process. Landf.* **46,** no. 11, 2195–2210, doi: 10.1002/esp.5168.

Doyle, E. E., S. J. Cronin, S. E. Cole, and J.-C. Thouret (2010). The coalescence and organization of lahars at Semeru volcano, Indonesia, *Bull. Volcanol.* **72,** 961–970, doi: 10.1007/s00445-010-0381-8.

Esri (2016). Ocean basemap, available at https://services.arcgisonline.com/ArcGIS/rest/services/Ocean/World_Ocean_Base/MapServer/tile/{z}/{y}/{x} (last accessed August 2026).

Farin, M., V. C. Tsai, M. P. Lamb, and K. E. Allstadt (2019). A physical model of the high-frequency seismic signal generated by debris flows, *Earth Surf. Process. Landf.* **44,** no. 13, 2529–2543, doi: 10.1002/esp.4677.

Farrell, J., S.-M. Wu, K. M. Ward, and F.-C. Lin (2018). Persistent noise signal in the FairfieldNodal three-component 5-Hz geophones, *Seismol. Res. Lett.* **89,** 1609–1617, doi: 10.1785/0220180073.

Gimbert, F., V. C. Tsai, and M. P. Lamb (2014). A physical model for seismic noise generation by turbulent flow in rivers, *J. Geophys. Res. Earth Surf.* **119,** no. 10, 2209–2238, doi: 10.1002/2014JF003201.

Hampton, M. A. (1975). Competence of fine–grained debris flows, *J. Sediment. Res.* **45,** no. 4, 834–844, doi: 10.1306/212F6E5B-2B24-11D7-8648000102C1865D.

Hoblitt, R. P., J. S. Walder, C. L. Driedger, K. M. Scott, P. T. Pringle, and J. W. Vallance (1998). Volcano hazards from Mount Rainier, Washington, revised 1998, *U.S. Geol. Surv. Open-File Rept. 98-428*.

Hsu, L., N. J. Finnegan, and E. E. Brodsky (2011). A seismic signature of river bedload transport during storm events, *Geophys. Res. Lett.* **38,** no. 13, doi: 10.1029/2011GL047759.

Huang, C., H. Yin, C. Chen, C. Yeh, and C. Wang (2007). Ground vibrations produced by rock motions and debris flows, *J. Geophys. Res. Earth Surf.* **112,** no. F02, doi: 10.1029/2005JF000437.

Iezzi, A. M., E. Bryant, W. A. Thelen, C. Gabrielson, S. C. Moran, M. R. Patrick, E. F. Younger, and M. K. Obryk (2024). Debris-flow monitoring on volcanoes via a novel usage of a laser rangefinder, *J. Appl. Volcanol.* **13,** no. 8, doi: 10.1186/s13617-024-00146-9.

Iverson, R. M. (1997). The physics of debris flows, *Rev. Geophys.* **35,** 245–296, doi: 10.1029/97RG00426.

Kean, J. W., J. A. Coe, V. Coviello, J. B. Smith, S. W. McCoy, and M. Arattano (2015). Estimating rates of debris flow entrainment from ground vibrations, *Geophys. Res. Lett.* **42,** 6365–6372, doi: 10.1002/2015GL064811.

Kelly, J. W., D. P. Siewiorek, A. Smailagic, and W. Wang (2016). An adaptive filter for the removal of drifting sinusoidal noise without a reference, *IEEE J. Biomed. Health. Inf.* **20,** no. 1, 213–221, doi: 10.1109/JBHI.2014.2375318.

Kramer, R. L., W. A. Thelen, A. M. Iezzi, S. C. Moran, and B. A. Pauk (2024). Recent expansion of the Cascades volcano observatory geophysical network at Mount Rainier for improved volcano and lahar monitoring, *Seismol. Res. Lett.* **95,** 2707–2721, doi: 10.1785/0220240112.

Lai, V. H., V. C. Tsai, M. P. Lamb, T. P. Ulizio, and A. R. Beer (2018). The seismic signature of debris flows: Flow mechanics and early warning at Montecito, California, *Geophys. Res. Lett.* **45,** no. 11, 5528–5535, doi: 10.1029/2018GL077683.

Lauge, D., N. Brodu, and J. Leroux (2013). Accurate 3D comparison of complex topography with terrestrial laser scanner: Application to the Rangitikei canyon (N-Z), *ISPRS J. Photogramm. Remote Sens.* **82,** 10–25.

Downloaded from pubs.geoscienceworld.org/ssa/srl/article-pdf/doi/10.1785/0220260021/8435001/srl-2026021.1.pdf by guest on 06 November 2026

Lee, G. R., R. Gommers, F. Waselewski, K. Wohlfahrt, and A. O'leary (2019). PyWavelets: A Python package for wavelet analysis, *J. Open Source Softw.* **4,** 1237, doi: 10.21105/joss.01237.

Márquez-Ramirez, V. H., L. Capra, J. I. Martínez-Valdés, R. Barroso-Fernández, R. Arámbula-Mendoza, M. González Amezcua, and R. García Flores (2025). Seismic classification of rainfall-induced lahars at Volcán de Colima, México: Frequency content as an indicator of sediment concentration, *J. South Am. Earth Sci.* **167,** 105768, doi: 10.1016/j.jsames.2025.105768.

Noh, M. J., and I. M. Howat (2017). The surface extraction from TIN based search-space minimization (SETSM) algorithm, *ISPRS J. Photogramm. Remote Sens.* **129,** 55–76, doi: 10.1016/j.isprsjprs.2017.04.019.

Pierson, T. C. (2005). Hyperconcentrated flow – transitional process between water flow and debris flow, in *Debris-flow Hazards and Related Phenomena*, M. Jakob and O. Hungr (Editors), Springer, Berlin, Heidelberg, 159–202.

Pierson, T. C., and J. E. Costa (1987). A rheologic classification of subaerial sediment–water flows, in *Debris Flows/Avalanches: Process, Recognition, and Mitigation*, J. E. Costa and G. F. Wieczorek (Editors), Vol. 7, Reviews in Engineering Geology, Geological Society of America, Boulder, Colorado, USA, 1–12.

Pierson, T. C., and K. M. Scott (1985). Downstream dilution of a Lahar: Transition from debris flow to hyperconcentrated streamflow, *Water Resour. Res.* **21,** 1511–1524, doi: 10.1029/WR021i010p01511.

QGIS.org (2024). QGIS geographic information system, available at https://www.qgis.org (last accessed February 2025).

Regalia, P. A. (1991). An improved lattice-based adaptive IIR notch filter, *IEEE Trans. Signal Process.* **39,** 2124–2128, doi: 10.1109/78.134453.

Ringler, A. T., R. E. Anthony, M. S. Karplus, A. A. Holland, and D. C. Wilson (2018). Laboratory tests of three Z–land fairfield nodal 5–Hz, three–component sensors, *Seismol. Res. Lett.* **89,** 1601–1608, doi: 10.1785/0220170236.

Schmandt, B., R. Aster, D. Scherler, V. Tsai, and K. Karlstrom (2013). Multiple fluvial processes detected by riverside seismic and infrasound monitoring of a controlled flood in the Grand Canyon, *Geophys. Res. Lett.* **40,** 4858–4863, doi: 10.1002/grl.50953.

Sisson, T. W., and J. W. Vallance (2009). Frequent eruptions of Mount Rainier over the last 2,600 years, *Bull. Volcanol.* **71,** 595–618, doi: 10.1007/s00445-008-0245-7.

Torrence, C., and G. P. Compo (1998). A practical guide to wavelet analysis, *Bull. Am. Meteorol. Soc.* **79,** 61–78, doi: 10.1175/1520-0477(1998)079<0061:APGTWA>2.0.CO;2.

Takahashi, T. (2014). *Debris Flow: Mechanics, Prediction and Countermeasures*, Second Ed., Taylow & Francis Group, London, UK.

Tsai, V. C., B. Minchew, M. P. Lamb, and J.-P. Ampuero (2012). A physical model for seismic noise generation from sediment transport in rivers, *Geophys. Res. Lett.* **39,** no. 2, L02404, doi: 10.1029/2011GL050255.

University of Oregon (2023). Mount Rainier 2023, doi: 10.7914/3wth-ea89.

University of Washington (2023). Pacific Northwest Seismic Network, University of Washington (PNSN), doi: 10.7914/SN/UW.

Walder, J. S., and C. L. Driedger (1995). Frequent outburst floods from South Tahoma Glacier, Mount Rainier, U.S.A.: Relation to debris flows, meteorological origin and implications for subglacial hydrology, *J. Glaciol.* **41,** 1–10, doi: 10.3189/S0022143000017718.

Walter, F., A. Burtin, B. W. McArdell, N. Hovius, B. Weder, and J. M. Turowski (2017). Testing seismic amplitude source location for fast debris-flow detection at Illgraben, Switzerland, *Nat. Hazards Earth Syst. Sci.* **17,** no. 6, 939–955, doi: 10.5194/nhess-17-939-2017.

Washington Geological Survey (2023). Rainier Wali 2022 Project, originally contracted by Washington Dept. of Natural Resources, available at https://lidarportal.dnr.wa.gov (last accessed April 2025).

Welch, P. D. (1967). The use of fast Fourier transform for the estimation of power spectra: A method based on time averaging over short, modified periodograms, *IEEE Trans. Audio Electroacoust.* **15,** no. 2, 70–73, doi: 10.1109/TAU.1967.1161901.

Wenner, M., F. Walter, B. McArdell, and D. Farinotti (2019). Deciphering debris-flow seismograms at Illgraben, Switzerland, *Debris-Flow Hazards Mitigation: Mechanics, Monitoring, Modeling, and Assessment-Proceedings of the 7th International Conference on Debris-Flow Hazards Mitigation*, Colorado School of Mines, 10–13.

Yang, Y., G. Chen, Y. Li, X. Meng, Y. Chong, S. Bian, J. Jin, W. Shi, J. Wu, and D. Yue (2024). Characterization of stream, hyperconcentrated and debris flows from seismic signals: Insights into sediment transport mechanisms and flow dynamics, *J. Geophys. Res. Earth Surf.* **129,** no. 4, e2023JF007527, doi: 10.1029/2023JF007527.

Zanuttigh, B., and A. Lamberti (2007). Instability and surge development in debris flows, *Rev. Geophys.* **45,** RG3006, doi: 10.1029/2005RG000175.

Zhang, Z., F. Walter, B. W. McArdell, T. de Haas, M. Wenner, M. Chmiel, and S. He (2021). Analyzing bulk flow characteristics of debris flows using their high frequency seismic signature, *J. Geophys. Res. Solid Earth* **126,** no. 12, e2021JB022755, doi: 10.1029/2021JB022755.

Manuscript received 15 January 2026
Published online 5 November 2026

Downloaded from pubs.geoscienceworld.org/ssa/srl/article-pdf/doi/10.1785/0220260021/8435001/srl-2026021.1.pdf by guest on 06 November 2026